

See discussions, stats, and author profiles for this publication at: <https://www.researchgate.net/publication/235639973>

# Evidence for the existence of oxygen clustering and understanding of structural disorder in Prussian blue analogues molecular magnet M<sub>1.5</sub>[Cr(CN)<sub>6</sub>]<sub>z</sub>H<sub>2</sub>O (M = Fe and Co) : reverse Mo...

## DATASET

---

CITATION

1

READS

27

## 5 AUTHORS, INCLUDING:



Pramod Bhatt

Bhabha Atomic Research Centre

67 PUBLICATIONS 181 CITATIONS

[SEE PROFILE](#)



Mayuresh Mukadam

Bhabha Atomic Research Centre

63 PUBLICATIONS 509 CITATIONS

[SEE PROFILE](#)



Sher Singh Meena

Bhabha Atomic Research Centre

150 PUBLICATIONS 525 CITATIONS

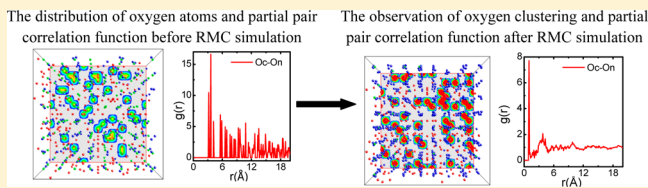
[SEE PROFILE](#)

# Evidence for the Existence of Oxygen Clustering and Understanding of Structural Disorder in Prussian Blue Analogues Molecular Magnet $M_{1.5}[Cr(CN)_6] \cdot zH_2O$ ( $M = Fe$ and $Co$ ): Reverse Monte Carlo Simulation and Neutron Diffraction Study

Pramod Bhatt,\* Nidhi Thakur,<sup>†</sup> Mayuresh D. Mukadam, Sher Singh Meena, and Seikh M. Yusuf

Solid State Physics Division, Bhabha Atomic Research Centre, Mumbai 400 085, India

**ABSTRACT:** A detailed structural disorder investigation of Prussian blue analogues  $M_{1.5}[Cr(CN)_6] \cdot zH_2O$  ( $M = Fe$  and  $Co$ ) has been done by carrying out a reverse Monte Carlo (RMC) simulation on the powder neutron diffraction data. X-ray diffraction, infrared spectroscopy, Mössbauer spectroscopy, and dc magnetization measurements have also been employed to investigate the structural and magnetic properties of the compounds. The Rietveld refinement of the X-ray and neutron diffraction patterns reveals that both compounds are in a single phase with a face-centered cubic crystal structure (space group  $Fm\bar{3}m$ ). The observation of characteristic absorption bands in the range  $1900$ – $2200$   $cm^{-1}$  of infrared (IR) spectra, which corresponds to the CN stretching frequency of  $M^{II}-N\equiv C-Cr^{III}$  sequence, confirms the formation of Prussian blue analogues,  $M_{1.5}[Cr(CN)_6] \cdot zH_2O$ . The IR study also infers the presence of cyanide flipping in the  $Fe_{1.5}[Cr(CN)_6] \cdot zH_2O$  compound. The Mössbauer study on the  $Fe_{1.5}[Cr(CN)_6] \cdot zH_2O$  compound confirms the presence of high as well as low spin  $Fe^{II}$  ions due to isomerization of some  $Cr^{III}-C\equiv N-Fe^{II}$  linkages to the  $Cr^{III}-N\equiv C-Fe^{II}$  form. The magnetization data show a soft ferromagnetic nature of both compounds with a Curie temperature of  $\sim 17$  and  $\sim 22$  K for  $Fe_{1.5}[Cr(CN)_6] \cdot zH_2O$  and  $Co_{1.5}[Cr(CN)_6] \cdot zH_2O$ , respectively. A large amount of structural disorder is present in both compounds, which is manifested in the form of a diffuse scattering in neutron diffraction patterns. The RMC results, obtained after the modeling, simulation, and analysis of the neutron diffraction data, propose that the water molecules and the  $[Cr(CN)_6]$  vacancies are mainly responsible for the structural disorder. Moreover, a clustering of the non-coordinated oxygen atoms around the coordinated oxygen atoms is also ascertained by the RMC analysis. The correlation of structural disorder with the water content and  $[Cr(CN)_6]$  vacancies is also discussed.



## INTRODUCTION

Periodic arrangements of atoms in a material decide the crystalline nature, and the local deviation of atoms from their atomic sites leads to the structural disorder in the materials. Structural disorder occurs due to an uncertainty in the spatial arrangements of atoms in a material. The disordered materials display interesting physical properties that are not always seen in their crystalline counterparts. Therefore, the disordered materials have also received great attention and are equally important from the scientific as well as technological point of view when compared to crystalline materials. For example, the disordered semiconductor materials, produced by metal doping, are highly useful in microelectronics technology.<sup>1</sup> Further, the high temperature superconductor can be synthesized with an optimal amount of doping of defects/disorder in the materials.<sup>2,3</sup> The disorder can be introduced in the materials either by using external stimuli, such as temperature, pressure, heat, magnetic field, or light, or intrinsically due to doping of atomic species, vacancies, impurities, defects, and flexing of molecules, and subsequently affects their physical properties.<sup>4–7</sup>

The physical properties of disordered materials mainly depend on the types of disorder (dynamic, static, and substitutional) present in the materials. Hence, a deeper understanding of local

structure/disorder at the atomic scale is highly desirable. Some examples of disordered materials<sup>8</sup> are (i) materials showing small deviation from perfect crystallinity: In–Ga–As semiconductor alloys,<sup>9,10</sup> (ii) crystalline materials showing significant structural disorder: nanophase LiMoS<sub>2</sub>,<sup>11</sup> (iii) completely disordered materials: Ca–Al–Si–O glasses,<sup>12</sup> (iv) materials showing no positional but chemical disorder: metallic Cu<sub>3</sub>Au,<sup>8</sup> (v) disorder in organic materials: ferrocene,<sup>13</sup> (vi) colossal magnetoresistance (CMR) materials with local dynamic distortions,<sup>14</sup> (vii) zeolites with host–guest systems,<sup>15,16</sup> and (viii) molecular disorder in C<sub>60</sub> and related compounds,<sup>17</sup> etc. In addition, one class of the crystalline materials which possesses structural disorder (static in nature) are Prussian blue analogues (PBA), which have attracted great attention recently because of their novel magnetic functionalities<sup>18</sup> as well as other properties, such as magnetic pole inversion,<sup>19,20</sup> photomagnetic behavior,<sup>21</sup> zero/negative thermal expansion,<sup>22</sup> etc. Moreover, these compounds are also the subject of increasing current interest because of the possibility of producing molecule-based magnets with ordering

Received: December 17, 2012

Revised: January 21, 2013

Published: January 22, 2013

**Table 1.** Elemental Analysis of  $M_{1.5}[Cr(CN)_6] \cdot zH_2O$  ( $M = Fe$  and  $Co$ ) Compounds

sample	elemental composition: the theoretically expected values, based on sample stoichiometry, are given in the bracket (wt %)			
	M	Cr	C	N
$Fe_{1.5}[Cr(CN)_6] \cdot 7H_2O$	21.2 (20.0)	11.2 (12.4)	16.1 (17.2)	19.8 (20.1)
$Co_{1.5}[Cr(CN)_6] \cdot 6H_2O$	20.8 (21.1)	13.5 (12.4)	18.8 (17.1)	20.7 (19.9)

temperature higher than room temperature<sup>23</sup> and their application in the storage of hydrogen.<sup>24,25</sup> PBAs are generally described with a common formula,  $X_pA_q[B(CN)_6]_r \cdot zH_2O$  in which  $A$  and  $B$  are transition metal ions and  $X$  are alkali metal ions, such as  $K^+$  and  $Rb^+$ . Generally,  $A$  ions exhibit a high spin state and  $B$  ions show a low spin state. The high spin and low spin ions are octahedrally surrounded by  $-N\equiv C-$  and  $-C\equiv N-$  units, respectively, in a face-centered cubic lattice, while alkali metal ions occupy the interstitial sites. The stoichiometry ( $q/r$  ratio) decides the  $B(CN)_6$  vacancies and the water content in the PBAs. The alkali ions, water molecules, and  $[B(CN)_6]$  vacancies constitute the structural defects in the PBAs and influence their physical properties. Therefore, a few attempts to characterize structural disorder phenomena in PBAs in correlation with magnetic properties have been undertaken.<sup>20,26,27</sup> For example, the photoinduced magnetization in PBAs is accompanied by the structural disorder (vacancies).<sup>28,29</sup> In another example, the  $RbMn[Fe(CN)_6] \cdot zH_2O$  compound shows a temperature and photoinduced phase transition, which is also accompanied by a structural transition from a face-centered cubic to tetragonal structure.<sup>30–32</sup> Moreover, the structural disorder reduces the number and/or uniformity of cyanide linkages, i.e., the exchange pathway between the transition metal ions in this  $RbMn[Fe(CN)_6] \cdot zH_2O$  compound. Experimentally, the structural disorder is probed with a diffuse scattering of X-rays or neutrons. In scattering experiments, the diffraction pattern of a crystalline material shows well-defined Bragg peaks, whereas a few Bragg peaks over a pronounced diffuse component are present in disordered materials. The refinement of such experimental diffraction data using the standard method like Rietveld<sup>33</sup> does not have the ability to introduce and analyze the structural disorder/diffuse scattering component. However, few other simulation methods,<sup>8,34–36</sup> such as molecular dynamics, atomic pair distribution function (PDF), and the reverse Monte Carlo (RMC) simulation methods, are available for investigating the structural disorder in materials. Among all, the RMC method<sup>36</sup> gives both the qualitative and quantitative information of the local structure of disordered materials. In this simulation method, no interatomic potential is required; thus, the structural model is actually fitted to the diffraction data. In the present work, we report a detailed structural disorder study of  $M_{1.5}[Cr(CN)_6] \cdot zH_2O$  ( $M = Fe$  and  $Co$ ) PBAs using a reverse Monte Carlo simulation on the neutron diffraction data. Also, we have explored the effects of structural disorder, due to the presence of vacancies of the  $Cr(CN)_6$  and water molecules, on the magnetic ordering in these compounds. In addition, the physical properties change with time due to the possibility of water uptake for this class of compounds, particularly  $Fe_{1.5}[Cr(CN)_6] \cdot zH_2O$ .

## EXPERIMENTAL SECTION

The polycrystalline samples of  $M_{1.5}[Cr(CN)_6] \cdot zH_2O$  ( $M = Fe$  and  $Co$ ) compounds were prepared using the coprecipitation method. The chemicals { $Fe(II)Cl_2$ ,  $Co(II)(NO_3)_2 \cdot 6H_2O$ , and  $K_3[Cr(CN)_6]$ } were reagent grade and used as received from Sigma-Aldrich. For the synthesis of  $Fe_{1.5}[Cr(CN)_6] \cdot zH_2O$ , required amounts of 0.15 and 0.1 M aqueous solutions (10 mL

each) of  $FeCl_2$  and  $K_3[Cr(CN)_6]$ , respectively, were prepared and heated separately up to 40 °C for 15 min. The prepared  $FeCl_2$  solution is thereafter mixed with the rapidly stirred aqueous solution of  $K_3[Cr(CN)_6]$  and heated up to 60 °C for 15 min. The precipitate of the required composition was formed. The precipitate was filtered, washed many times with doubly distilled water and ethanol, and finally allowed to dry in air. Similarly, the  $Co_{1.5}[Cr(CN)_6] \cdot zH_2O$  compound was synthesized by mixing of  $Co(NO_3)_2$  and  $K_3[Cr(CN)_6]$  chemicals, as described above. The stoichiometry of the compounds was confirmed by chemical analysis: (i) trace elemental analysis (flame atomic absorption spectroscopy, FAAS) for  $Fe$ ,  $Co$ , and  $Cr$  with an accuracy of ~0.2% and (ii) the combustion gas chromatographic method for  $C$  and  $N$  with an accuracy of ~0.5 and 5%, respectively. The results of the elemental analysis are given in Table 1.

The X-ray diffraction (XRD) measurements were performed at room temperature (~25 °C) in a Bragg–Brentano geometry using a Rigaku diffractometer over an angular ( $2\theta$ ) range of 10–70° in equal  $2\theta$  steps of 0.02° using a  $Cu K\alpha$  radiation. A detailed structural analysis is performed on the XRD data by the Rietveld refinement method with the Fullprof software.<sup>37</sup> The neutron diffraction patterns were recorded using a wavelength of  $\lambda = 1.249 \text{ \AA}$  at 300 and 6 K on five linear position-sensitive detectors (PSD) based powder diffractometer-II at the Dhruva reactor, Trombay, India.

For further structural characterization of the PBAs, the infrared (IR) spectra were recorded in the range 1900–2300  $\text{cm}^{-1}$  by loading the samples in a KBr pellet on a Bruker VERTEX 80v Fourier transform infrared spectrometer.

Mössbauer spectra were recorded for the  $Fe_{1.5}[Cr(CN)_6] \cdot zH_2O$  sample using a Mössbauer spectrometer (Nucleonix Systems Pvt. Ltd., Hyderabad, India) operated in constant acceleration mode (triangular wave) in transmission geometry at room temperature (~25 °C). The source employed was  $Co-57$  in Rh matrix of strength 50 mCi. The calibration of the velocity scale was done by using an enriched  $\alpha-^{57}Fe$  metal foil. The line width (inner) of calibration spectra was 0.23 mm/s.

The magnetization measurements were carried out using a Cryogenic, UK make commercial magnetic properties measurements system as a function of both temperature and magnetic field. The temperature dependent magnetization measurements were carried out in zero-field-cooled (ZFC) and field-cooled (FC) conditions down to 5 K. For the ZFC measurements, the sample was cooled from room temperature down to the lowest temperature in the absence of a magnetic field, and magnetization was measured in the warming cycle with the applied magnetic field on, whereas, in the FC measurements, the sample was cooled from room temperature down to the lowest temperature in the presence of an applied magnetic field and the magnetization was measured in the warming cycle under the same field. Hysteresis curves were recorded at 5 K over +90 to −90 kOe applied magnetic field for  $M_{1.5}[Cr(CN)_6] \cdot zH_2O$  ( $M = Fe$  and  $Co$ ) compounds.

## ■ DESCRIPTION AND FORMALISM OF RMC MODELING

The programs generally used for crystal structural refinement (including the Rietveld method) provide information about space group symmetry, lattice parameters, and average atomic positions within the unit cell, etc. These programs totally rely on Bragg peak intensities and positions. However, such programs have limited flexibility to accommodate local structural variations {occurring due to thermal vibrations, substitutional disorder, and crystal defects (vacancies), etc.}, leading to changes in Bragg peak intensities and positions. The presence of structural disorder in crystalline materials leads to the presence of diffuse scattering intensity over Bragg intensity in diffraction data. Diffraction data containing diffuse scattering can be analyzed in many ways, depending on the type of disorder responsible for the diffuse scattering. In the case where the scattering data are limited due to complex and substantial disorder, the molecular dynamics computer simulation has been used extensively.<sup>38</sup> However, where the disorder is intrinsic, the RMC modeling {based on the variation of the standard Metropolis Monte Carlo (MMC) method<sup>39</sup>} plays an important role to access structural details that are not straightforward to extract using other methods.

The basic idea of the RMC and its algorithm has been described earlier in the literature.<sup>36,40–42</sup> In RMC modeling, a structural model of  $N$  atoms is generated and is tried to match with that generated from experimental diffraction data. The  $N$  atoms are placed in a super cell of a crystalline unit cell with periodic boundary conditions. The cell geometry, size, and positions of atoms in coordinates are known as a configuration. The positions of the atoms may be chosen randomly; they may have a known crystal structure, or they may be taken from a different simulation or model. The pair correlation functions  $\{g_{ij}^{\text{cal}}(r)\}$  are then calculated for this initial configuration cell using the following expression:

$$g_{ij}^{\text{cal}}(r) = \frac{n_{ij}^{\text{cal}}(r)}{4\pi r^2 d\rho(r)} \quad (1)$$

where  $n_{ij}^{\text{cal}}(r)$  is the number of atoms of type “ $i$ ” situated at a distance  $r$  and  $r + dr$  from a central atom “ $j$ ”.  $\rho(r)$  is the atomic number density at distance  $r$ . The partial structure factor is calculated using the Fourier transform of the pair correlation functions  $\{g_{ij}^{\text{cal}}(r)\}$ .

$$P_{\text{initial}}^{\text{cal}}(Q) = \rho \int_{\infty}^0 4\pi r^2 \{g_{ij}^{\text{cal}}(r) - 1\} \frac{\sin Qr}{Qr} dr \quad (2)$$

where  $Q$  is the momentum transfer vector. The total structure factor is calculated using

$$S_{\text{initial}}^{\text{cal}}(Q) = \sum P^{\text{cal}}(Q) - 1 \quad (3)$$

where the summation is over all the atoms.

Then, finally the difference between the experimentally observed total structure factor,  $S^{\text{exp}}(Q)$ , and that determined from the *initial* configuration,  $S^{\text{cal}}(Q)$ , is calculated using

$$\chi_{\text{initial}}^2 = \sum_{z=1}^m \frac{\{S^{\text{cal}}(Q_m) - S^{\text{exp}}(Q_m)\}^2}{\sigma^2} \quad (4)$$

where the summation is over  $m$  experimental data points and  $\sigma$  is the experimental error. The minimum  $Q_m$  value used should be larger than or equal to  $2\pi/L$ , where  $L$  is the minimum dimension of the configuration. After calculating  $\chi_{\text{initial}}^2$ , atoms are allowed to

move randomly in the configuration. However, if any two atoms approach closer than a predefined (cutoff) distance, then the move is rejected and a new atom is chosen for a new move. The new total structure factors,  $\{S^{\text{cal}}(Q)\}$ , and the difference  $\chi_{\text{move}}^2$  are calculated for the configuration of atoms of given moves. If  $\chi_{\text{initial}}^2 > \chi_{\text{move}}^2$ , the move is accepted and the new configuration becomes the initial one, and when  $\chi_{\text{move}}^2 > \chi_{\text{initial}}^2$ , the move is accepted with the probability of  $\exp\{-(\chi_{\text{move}}^2 - \chi_{\text{initial}}^2)/2\}$  or otherwise rejected. The above process is continued until a good fit between the experimental and calculated structure factors is obtained. In the present study, we have used the RMCPow program<sup>43,44</sup> to investigate the diffuse scattering in the neutron diffraction data of  $M_{1.5}[\text{Cr}(\text{CN})_6] \cdot z\text{H}_2\text{O}$  compounds. The RMC analysis of the neutron diffraction data is discussed in detail in the next section.

## ■ RESULTS AND DISCUSSION

**A. X-ray Diffraction Study.** Figure 1 presents the Rietveld refined (using the FULLPROF program)<sup>37</sup> room temperature X-

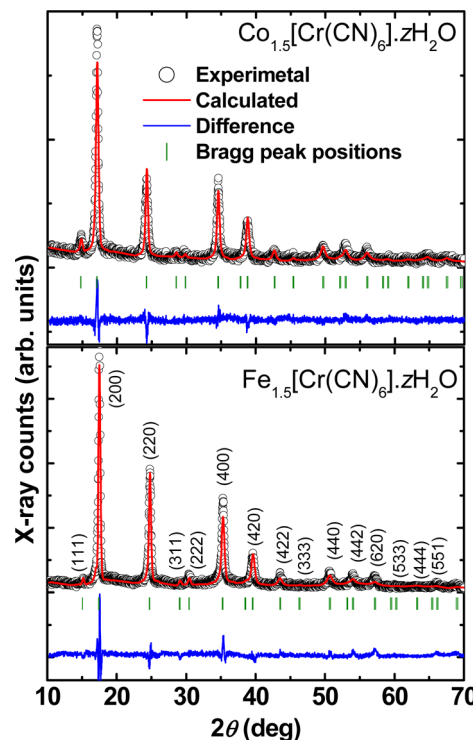


**Figure 1.** Rietveld refined room temperature XRD patterns of  $M_{1.5}[\text{Cr}(\text{CN})_6] \cdot z\text{H}_2\text{O}$  ( $M = \text{Fe}$  and  $\text{Co}$ ) PBAs. Open circles and solid lines indicate the observed and the calculated patterns, respectively. Solid lines at the bottom show the difference between observed and calculated patterns. Vertical lines at the bottom of XRD patterns show the position of allowed Bragg peaks. The  $(hkl)$  values of corresponding Bragg peaks are also marked for  $\text{Fe}_{1.5}[\text{Cr}(\text{CN})_6] \cdot z\text{H}_2\text{O}$ .

ray powder diffraction patterns of  $M_{1.5}[\text{Cr}(\text{CN})_6] \cdot z\text{H}_2\text{O}$  ( $M = \text{Fe}$  and  $\text{Co}$ ) compounds. It is evident from the derived results of the fitted XRD patterns that the compounds are in the single crystalline phase. The structure of the compound is face-centered cubic (fcc) with space group  $Fm\bar{3}m$ . In the fcc structure, the transition metal ions ( $M^{II}$ ) are located at the  $4a(0, 0, 0)$  crystallographic position, while the  $\text{Cr}^{III}$  ions occupy the  $4b(1/2, 1/2, 1/2)$  crystallographic position. The important structural parameters, such as atomic coordinates and site occupancies,

**Table 2. Structural Parameters of Rietveld Refined X-ray Diffraction Patterns of  $M_{1.5}[Cr(CN)_6] \cdot zH_2O$  ( $M = Fe$  and  $Co$ ) Compounds. ( $x'$ ,  $y'$ , and  $z'$  Denote the Fractional Coordinates)**

M	atom	Wyckoff site	$x'$	$y'$	$z'$	occupancy
Fe	Fe	4a	0.0	0.0	0.0	1.5
	Cr	4b	0.5	0.5	0.5	1.0
	C	24e	0.31(1)	0.0	0.0	6.0
	N	24e	0.23(7)	0.0	0.0	6.0
	O1	24e	0.20(9)	0.0	0.0	3.0
	O2	32f	0.28(8)	0.28(8)	0.28(8)	2.3(4)
	O3	8c	0.25	0.25	0.25	1.7(3)
Co	Co	4a	0.0	0.0	0.0	1.5
	Cr	4b	0.5	0.5	0.5	1.0
	C	24e	0.31(7)	0.0	0.0	6.0
	N	24e	0.21(3)	0.0	0.0	6.0
	O1	24e	0.19(4)	0.0	0.0	3.0
	O2	32f	0.30(6)	0.30(6)	0.30(6)	1.4(2)
	O3	8c	0.25	0.25	0.25	1.2(3)

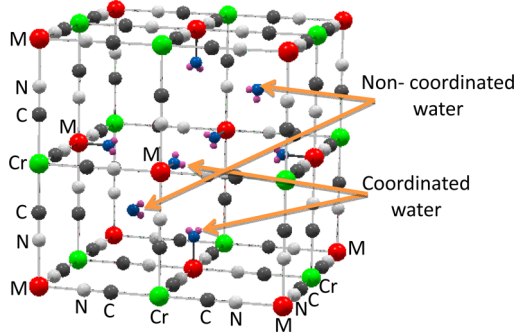


**Figure 2.** The unit cell structure of the  $M_{1.5}[Cr(CN)_6] \cdot zH_2O$  compound. The structure shows the water molecules are coordinated to a metal ion (M), due to creation of  $Cr(CN)_6$  vacancies. The non-coordinated water molecules residing at 8c interstitial sites are also shown.

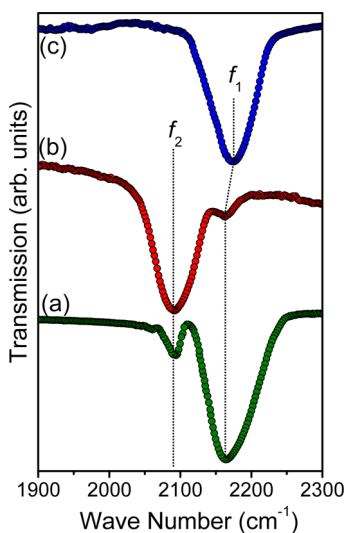


**Figure 3.** Room temperature IR spectra for (a)  $Fe_{1.5}[Cr(CN)_6] \cdot zH_2O$  and (c)  $Co_{1.5}[Cr(CN)_6] \cdot zH_2O$  compounds. Part b shows the IR spectrum recorded after 2 months again on the same compound,  $Fe_{1.5}[Cr(CN)_6] \cdot zH_2O$ . Two absorption bands  $f_1$  and  $f_2$  are guided by dotted lines for better visibility.

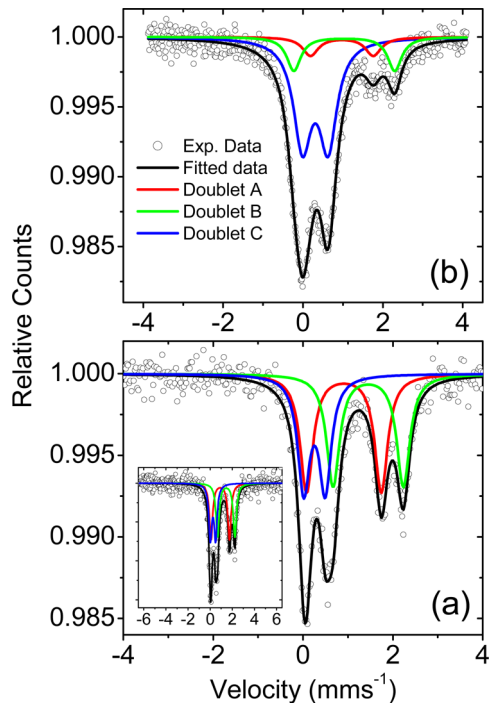


**Figure 4.** (a) Mössbauer spectrum of the  $Fe_{1.5}[Cr(CN)_6] \cdot zH_2O$  compound at room temperature. The inset shows the spectrum recorded up to  $\pm 6.5$  mm/s velocity. (b) Mössbauer spectrum of the  $Fe_{1.5}[Cr(CN)_6] \cdot zH_2O$  compound, recorded after 2 months of sample preparation. Open circles show the experimental data, and the thick solid line is the least-squares fitted curve.

derived from the Rietveld analysis, are shown in Table 2. The lattice parameters are found to be  $\sim 10.18(9)$  and  $10.38(3)$  Å for  $Fe_{1.5}[Cr(CN)_6] \cdot zH_2O$  and  $Co_{1.5}[Cr(CN)_6] \cdot zH_2O$  compounds, respectively. It is found that the water molecules reside at coordinated sites (24e) as well as interstitial sites (8c and 32f). The number of total water molecules in  $M_{1.5}[Cr(CN)_6] \cdot zH_2O$  compounds is estimated from the derived number of oxygen atoms, obtained from the Rietveld refinement of the X-ray diffraction patterns shown in Figure 1. In general, two types of water molecules, i.e., coordinated and non-coordinated, may be present in  $A_q[B(CN)_6]_r \cdot zH_2O$  PBA compounds depending on their stoichiometry (ratio  $q/r$ ). When  $q/r = 1$ , no  $[B(CN)_6]$  vacancies are present in the structure and only non-coordinated water molecules occupying the interstitial positions of 8c and 32f. However, when  $q/r > 1$  (i.e., the case for the present  $M_{1.5}[Cr(CN)_6] \cdot zH_2O$  compounds),  $B(CN)_6$  vacancies are present in the compound and both types of water molecules (coordinated and non-coordinated) are present in the structure (as shown in Figure 2). In the studied compounds, the Cr (4b), C (24e), and N (24e) sites are partially occupied; i.e., vacancies of  $[Cr(CN)_6]$  units are present in the structure. The coordinated water molecules reside at empty nitrogen sites.

**B. Infrared and Mössbauer Spectroscopy Study.** The IR spectra of both compounds, in the spectral range 1900–2300 cm<sup>-1</sup>, are shown in Figure 3. This spectral range belongs to the stretching frequencies of the CN ligand in PBAs. The stretching frequency of the free (CN) molecular ion in an aqueous solution is observed at 2080 cm<sup>-1</sup>. However, with the formation of the A—N≡C bridge, it is shifted to a higher frequency side.<sup>45</sup> Therefore, one can easily probe the formation of the PBAs by following the frequencies associated with the CN bridging ligand. Parts a and c of Figure 3 show IR spectra of  $Fe_{1.5}[Cr(CN)_6] \cdot zH_2O$  recorded at room temperature and after 2 months, respectively. The IR spectrum of  $Co_{1.5}[Cr(CN)_6] \cdot zH_2O$  is also shown in Figure 3(c). The IR spectra of the studied compounds show two strong absorption bands at approximately 2080 and 2100 cm<sup>-1</sup>, which are assigned to the CN stretching frequencies. The intensity of the 2080 cm<sup>-1</sup> band decreases significantly after 2 months, indicating the formation of the CN bridging ligand in the structure.

Table 3. Hyperfine Parameters (Extracted from Mössbauer Spectra) for the  $\text{Fe}^{\text{II}}_{1.5}[\text{Cr}^{\text{III}}(\text{CN})_6] \cdot z\text{H}_2\text{O}$  Compound

sample	doublet	spin state of $\text{Fe}^{2+}$ ion	quadrupole splitting ( $\Delta E_Q$ , mm/s)	isomer shift ( $\delta$ , mm/s)	line width ( $\Gamma$ , mm/s)	area ( $R_A$ , %)
$\text{Fe}_{1.5}[\text{Cr}(\text{CN})_6] \cdot z\text{H}_2\text{O}$	A	HS	$1.664 \pm 0.018$	$0.911 \pm 0.009$	$0.348 \pm 0.024$	35.6
	B	HS	$1.564 \pm 0.011$	$1.452 \pm 0.006$	$0.352 \pm 0.019$	34.5
	C	LS	$0.478 \pm 0.018$	$0.255 \pm 0.009$	$0.326 \pm 0.024$	29.9
$\text{Fe}_{1.5}[\text{Cr}(\text{CN})_6] \cdot z\text{H}_2\text{O}$ (recorded after 2 months)	A	HS	$2.526 \pm 0.049$	$0.974 \pm 0.018$	$0.483 \pm 0.072$	10.5
	B	HS	$1.573 \pm 0.027$	$1.034 \pm 0.011$	$0.427 \pm 0.044$	15.0
	C	LS	$0.643 \pm 0.007$	$0.308 \pm 0.003$	$0.543 \pm 0.012$	74.5

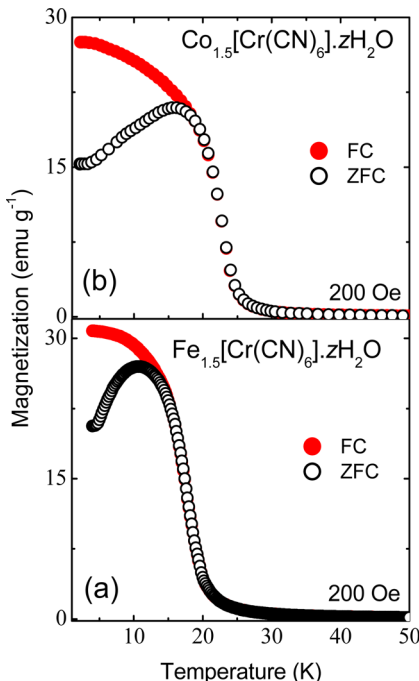


Figure 5. Field-cooled (FC) and zero-field-cooled (ZFC) magnetization versus temperature ( $T$ ) curves measured at 200 Oe field for (a)  $\text{Fe}_{1.5}[\text{Cr}(\text{CN})_6] \cdot z\text{H}_2\text{O}$  and (b)  $\text{Co}_{1.5}[\text{Cr}(\text{CN})_6] \cdot z\text{H}_2\text{O}$  compounds.

(CN)<sub>6</sub>]·zH<sub>2</sub>O and Co<sub>1.5</sub>[Cr(CN)<sub>6</sub>]·zH<sub>2</sub>O compounds, respectively. Two absorption bands ( $f_1$  and  $f_2$ ) are visible for the  $\text{Fe}_{1.5}[\text{Cr}(\text{CN})_6] \cdot z\text{H}_2\text{O}$  compound. The pronounced  $f_1$  band centered at 2168 cm<sup>-1</sup> is attributed to the cyanide stretching frequency of  $\text{Fe}^{\text{II}}-\text{N}\equiv\text{C}-\text{Cr}^{\text{III}}$ . In addition, another absorption band of smaller intensity ( $f_2$ ), centered at 2090 cm<sup>-1</sup>, is attributed to  $\text{Fe}^{\text{II}}-\text{C}\equiv\text{N}-\text{Cr}^{\text{III}}$ , which is due to a small fraction of flipping of the cyano (CN) ligand. The cyano-flip phenomenon is explained by the linkage isomerism in which iron(II) hexacyanochromate(III) {Cr<sup>III</sup>—C≡N—Fe<sup>II</sup> (high spin)} is transformed into the more stable chromium(III) hexacyanoferrate(II) {Cr<sup>III</sup>—N≡C—Fe<sup>II</sup> (low spin)} on heating or standing at room temperature for several months with an obvious color change from brick red to green.<sup>46–48</sup> This fact is confirmed by recording the IR spectra of the  $\text{Fe}_{1.5}[\text{Cr}(\text{CN})_6] \cdot z\text{H}_2\text{O}$  compound after 2 months (Figure 3b). It can be seen that the intensity of  $f_1$  decreases and  $f_2$  increases due to the transformation of Cr<sup>III</sup>—C≡N—Fe<sup>II</sup> to Cr<sup>III</sup>—N≡C—Fe<sup>II</sup>. This kind of CN flipping has been reported in many PBAs, e.g., (Co<sub>x</sub>Ni<sub>1-x</sub>)<sub>1.5</sub>[Fe(CN)<sub>6</sub>]<sup>49</sup>, (Cu<sub>x</sub>Mn<sub>1-x</sub>)<sub>1.5</sub>[Fe(CN)<sub>6</sub>]<sup>20</sup>, Fe[Cr(CN)<sub>6</sub>]<sup>50</sup> and Fe[Mn(CN)<sub>6</sub>]·zH<sub>2</sub>O.<sup>51</sup> The flipping of cyano molecules is a structural defect and leads to disorder in the material. The IR spectrum of the Co<sub>1.5</sub>[Cr(CN)<sub>6</sub>]·zH<sub>2</sub>O compound shows a single band ( $f_1$ ), centered at 2172 cm<sup>-1</sup>.

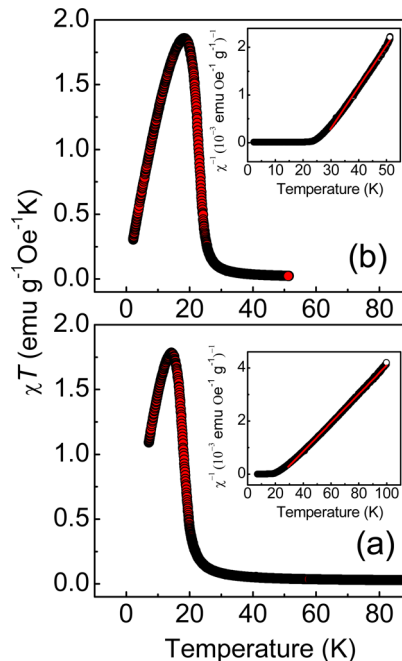
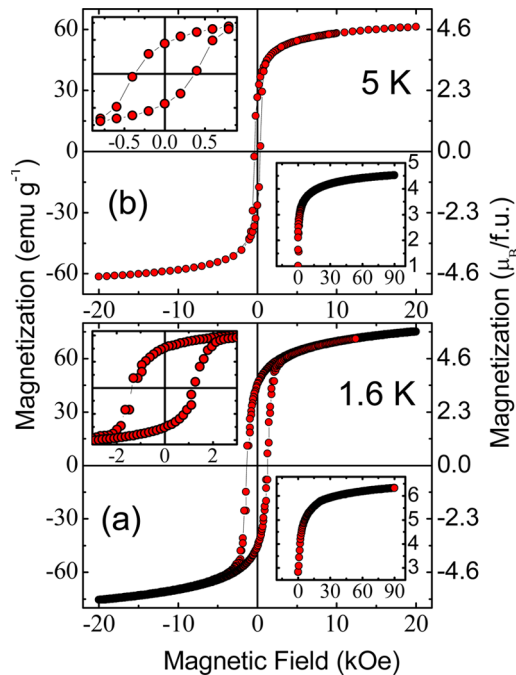


Figure 6.  $\chi T$  vs temperature curves measured in an applied field of 200 Oe for (a)  $\text{Fe}_{1.5}[\text{Cr}(\text{CN})_6] \cdot z\text{H}_2\text{O}$  and (b)  $\text{Co}_{1.5}[\text{Cr}(\text{CN})_6] \cdot z\text{H}_2\text{O}$  compounds. The inverse susceptibility vs temperature curves are shown in the insets of corresponding figures and fitted by using the Curie–Weiss law.

The  $f_1$  band is attributed to Co<sup>II</sup>—N≡C—Cr<sup>III</sup>. It should be noted that we have not observed any significant decrease in the intensity of the  $f_1$  band or the appearance of the new band in the IR spectra of the Co<sub>1.5</sub>[Cr(CN)<sub>6</sub>]·zH<sub>2</sub>O compound recorded again after 2 months, suggesting that the CN flipping does not occur in this compound. The values of CN stretching frequencies for both M<sub>1.5</sub>[Cr(CN)<sub>6</sub>]·zH<sub>2</sub>O compounds are close to previously reported CN stretching frequencies of PBAs.<sup>47,48,52–55</sup> Thus, the characteristic absorption bands of the observed CN stretching frequencies confirm the formation of M<sub>1.5</sub>[Cr(CN)<sub>6</sub>]·zH<sub>2</sub>O compounds.

In order to confirm the cyano flipping phenomenon and the presence of the high spin and low spin state of Fe ions in the  $\text{Fe}_{1.5}[\text{Cr}(\text{CN})_6] \cdot z\text{H}_2\text{O}$  compound, a Mössbauer spectroscopic study has been carried out. The local magnetic environment around the Fe ions is analyzed from the Mössbauer spectra, recorded at a velocity of 6.5 mm/s. A room temperature Mössbauer spectrum of the  $\text{Fe}_{1.5}[\text{Cr}(\text{CN})_6] \cdot z\text{H}_2\text{O}$  compound is shown in Figure 4a. No magnetic hyperfine pattern is observed in the Mössbauer spectrum (the inset shows an absence of six line hyperfine pattern at higher velocity, confirming its paramagnetic nature at room temperature). The fitting of the data indicates the presence of three paramagnetic symmetric doublets (A, B, and



**Figure 7.** Magnetization ( $M$ ) vs field ( $H$ ) curves for (a)  $\text{Fe}_{1.5}[\text{Cr}(\text{CN})_6] \cdot z\text{H}_2\text{O}$  at 1.6 K and (b)  $\text{Co}_{1.5}[\text{Cr}(\text{CN})_6] \cdot z\text{H}_2\text{O}$  at 5 K. The upper inset shows the magnified view of  $M$  vs  $H$  curves, and the lower inset shows the virgin  $M$  vs  $H$  curves up to 90 KOe field.

C), suggesting that Fe ions have three different surrounding environments. The hyperfine parameters extracted from fitted Mössbauer spectra are given in Table 3. These three different surrounding environments of Fe ions in the  $\text{Fe}_{1.5}^{II}[\text{Cr}^{III}(\text{CN})_6] \cdot z\text{H}_2\text{O}$  compound can be understood from the structural point of view. From the crystal structure shown in Figure 2, it may be noted that the Fe ions are surrounded by the N octahedra, resulting in the high spin state of the Fe ion. However, in the case of cyano flipping, some Fe ions are surrounded by the C instead of N atoms which leads to a low spin state of Fe. In the third surrounding environment, the high spin Fe ions are also coordinated to two water molecules along with four N atoms. The quadrupole splitting ( $\Delta E_Q$ ) values of the three doublets are found to be 1.664, 1.564, and 0.478 mm/s, respectively. Two doublets (A and B) are having a comparatively high  $\Delta E_Q$  value; this shows more asymmetry around Fe ions. The corresponding isomer shift values ( $\delta$ ) are found to be 0.911, 1.452, and 0.255 mm/s. The doublets with  $\delta$  values of 0.911 and 1.452 mm/s belong to  $\text{Fe}^{2+}$  ions in the high spin (HS) state, whereas the doublet with a  $\delta$  value of 0.255 mm/s belongs to  $\text{Fe}^{2+}$  ions in the low spin (LS) state configuration.<sup>56</sup> The areas under the doublets A, B, and C (Table 3) give a direct estimation that 70.1% of  $\text{Fe}^{2+}$  ions are in the HS state while the remaining 29.9% are in the LS state. To determine the effect of time on spin states of  $\text{Fe}^{2+}$  ions, the Mössbauer spectrum has been recorded again on the same  $\text{Fe}_{1.5}^{II}[\text{Cr}^{III}(\text{CN})_6] \cdot z\text{H}_2\text{O}$  compound after 2 months (Figure 4b). It is found that the values of  $\Delta E_Q$  and line width increase for all three doublets which show an increase in asymmetry around the Fe nucleus. By calculating the area under the doublets, it is found that 10.5% of  $\text{Fe}^{2+}$  ions are in the HS state, while the remaining 89.5% are in the LS state. The drastic change in percentage of HS and LS  $\text{Fe}^{2+}$  ions with time further confirms the cyanide flipping (transformation of  $\text{Cr}^{III}-\text{C}\equiv\text{N}-\text{Fe}^{II}$  to  $\text{Cr}^{III}-\text{N}\equiv\text{C}-\text{Fe}^{II}$ ) in the  $\text{Fe}_{1.5}^{II}[\text{Cr}^{III}(\text{CN})_6] \cdot z\text{H}_2\text{O}$  compound, as already deduced by IR study.

**C. dc Magnetization Study.** Field-cooled (FC) and zero-field-cooled (ZFC) magnetization versus temperature ( $T$ ) curves at 200 Oe field for  $\text{M}_{1.5}[\text{Cr}(\text{CN})_6] \cdot z\text{H}_2\text{O}$  ( $\text{M} = \text{Fe}$  and  $\text{Co}$ ) compounds are shown in Figure 5. Both compounds show a magnetic transition below their respective transition temperatures. The magnetic transition is ferromagnetic in nature, which is discussed later in the text. The values of Curie temperature ( $T_C$ ), derived from the corresponding  $dM/dT$  versus  $T$  curve, are  $\sim 17$  and  $\sim 22$  K for  $\text{Fe}_{1.5}^{II}[\text{Cr}^{III}(\text{CN})_6] \cdot z\text{H}_2\text{O}$  and  $\text{Co}_{1.5}^{II}[\text{Cr}^{III}(\text{CN})_6] \cdot z\text{H}_2\text{O}$  compounds, respectively. A branching in the FC and ZFC magnetization curves has been observed for both compounds, which can be discussed in terms of the formation of magnetic domains and the domain wall motion under various cooling conditions.<sup>49,57</sup> In the ZFC process, i.e., when the field is zero, the magnetic domains are randomly disordered in the compound at room temperature, showing zero magnetization. When the sample is cooled in a field, the spin moments are ordered, and almost parallel to the direction of applied field. The cooling of the sample under a magnetic field would favor the growth of domains in the direction of the applied magnetic fields, and hence, it would result in a higher value of magnetization as compared to the ZFC magnetization. In addition, for the systems having long-range magnetic ordering, the branching can also occur due to inhomogeneities and disorder.<sup>58,59</sup>

The  $\chi T$  vs  $T$  ( $\chi$  is the dc magnetic susceptibility) curves for  $\text{M}_{1.5}[\text{Cr}(\text{CN})_6] \cdot z\text{H}_2\text{O}$  compounds are shown in Figure 6. The  $\chi T$  vs  $T$  curves show characteristics of ferromagnetism; i.e., the  $\chi T$  values for both samples rise slowly up to a certain temperature, and after that, they shoot up sharply, showing a maximum value of  $\chi T$ , and then decrease as the temperature is decreased further. The temperature dependence of the inverse of the susceptibility ( $\chi^{-1}$ ), shown in the inset of Figure 6, can be described and fitted by the straight line using the Curie–Weiss law.

$$\chi = \frac{C}{T - \theta_p}$$

where  $C$  is the Curie constant and  $\theta_p$  is the paramagnetic Curie temperature. The positive values of  $\theta_p$  (24 and 26 K for  $\text{Fe}_{1.5}[\text{Cr}(\text{CN})_6] \cdot z\text{H}_2\text{O}$  and  $\text{Co}_{1.5}[\text{Cr}(\text{CN})_6] \cdot z\text{H}_2\text{O}$  compounds, respectively) confirm the ferromagnetic nature of both compounds. The spin only effective paramagnetic moments,  $\mu_{\text{eff}}$  {6.4 and 5.9  $\mu_B$ /f.u. for the  $\text{Fe}_{1.5}[\text{Cr}(\text{CN})_6] \cdot z\text{H}_2\text{O}$  and  $\text{Co}_{1.5}[\text{Cr}(\text{CN})_6] \cdot z\text{H}_2\text{O}$  compounds, respectively} are calculated by using the formula  $\mu_{\text{eff}} = (3Ck_B/N_A)^{1/2}\mu_B \sim (8C)^{1/2}\mu_B$  where  $N_A$  is Avogadro's number and  $k_B$  is the Boltzmann constant. The theoretically expected (spin only) values of  $\mu_{\text{eff}}$  are also calculated by using the formula  $(\mu_{\text{eff}})^2 = \sum [g^2 \{n \cdot S(S+1)\}] \mu_B^2$ , where  $g$  is the gyromagnetic ratio ( $\sim 2$ ),  $n$  is the number of magnetic ions with spin  $S$  in the formula unit, and the summation  $\sum$  runs over all magnetic ions in the formula unit. The theoretically calculated values of spin only  $\mu_{\text{eff}}$  are found to be 7.1 and 6.1  $\mu_B$ /f.u. for the  $\text{Fe}_{1.5}[\text{Cr}(\text{CN})_6] \cdot z\text{H}_2\text{O}$  and  $\text{Co}_{1.5}[\text{Cr}(\text{CN})_6] \cdot z\text{H}_2\text{O}$  compounds, respectively, assuming metal ions ( $\text{M}$ ) in their high spin states. However, in the  $\text{Fe}_{1.5}[\text{Cr}(\text{CN})_6] \cdot z\text{H}_2\text{O}$  compound, 70.1% Fe ions are in the high spin state, while 29.9% are in the low spin state as obtained from Mössbauer study. The theoretically calculated spin only values of  $\mu_{\text{eff}}$  should be, therefore,  $[2^2 \{1.5 \times 2 \times (2+1) \times 0.70 + 1.5 \times 0 \times (0+1) \times 0.29 + 1 \times 3/2 \times (3/2+1)\}]^{1/2}\mu_B = 6.3\mu_B$  for the  $\text{Fe}_{1.5}[\text{Cr}(\text{CN})_6] \cdot z\text{H}_2\text{O}$  compound. The theoretically calculated values of spin only  $\mu_{\text{eff}}$  are consistent with

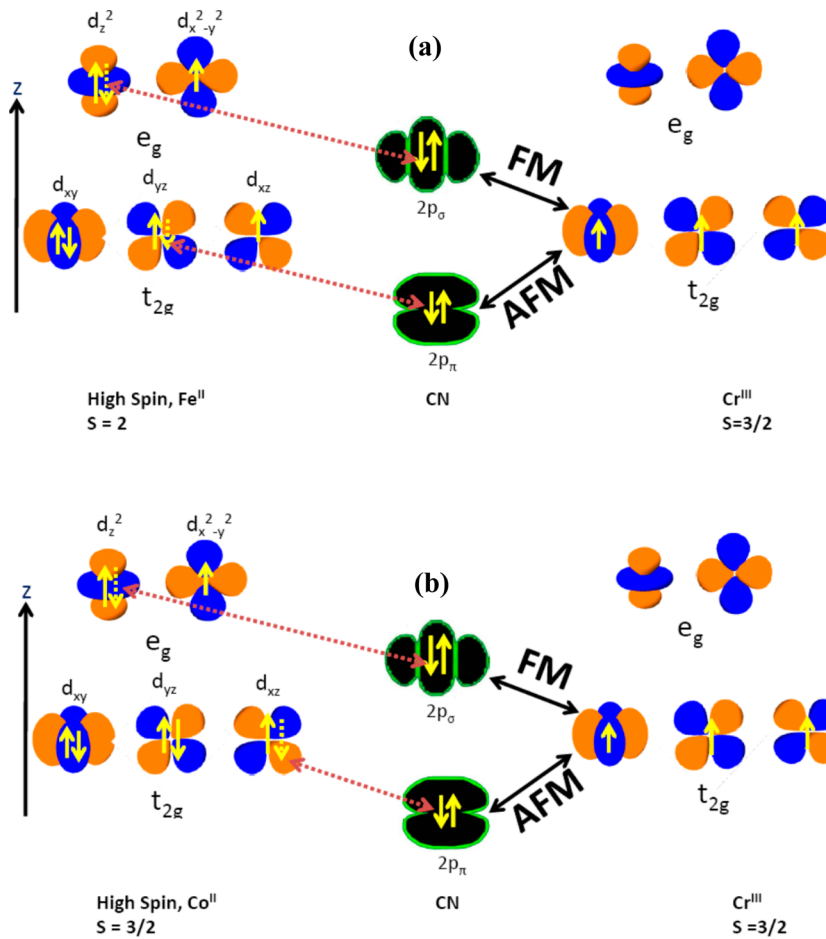


**Figure 8.** Schematic diagram of the super exchange interaction between metal (M) and Cr ions through CN ligand in (a)  $\text{Fe}_{1.5}[\text{Cr}(\text{CN})_6]\cdot z\text{H}_2\text{O}$  and (b)  $\text{Co}_{1.5}[\text{Cr}(\text{CN})_6]\cdot z\text{H}_2\text{O}$  compounds. The possible electron transfers between the orbitals ( $e_g$ ,  $t_{2g}$  of  $\text{M}^{\text{II}}$  ions and  $2p_{\pi}$ ,  $2p_{\sigma}$  of CN ligand) are shown by dotted lines. The ferromagnetic (FM) and antiferromagnetic (AFM) exchange interactions between metal (M) ions and Cr ions are shown by solid black lines.

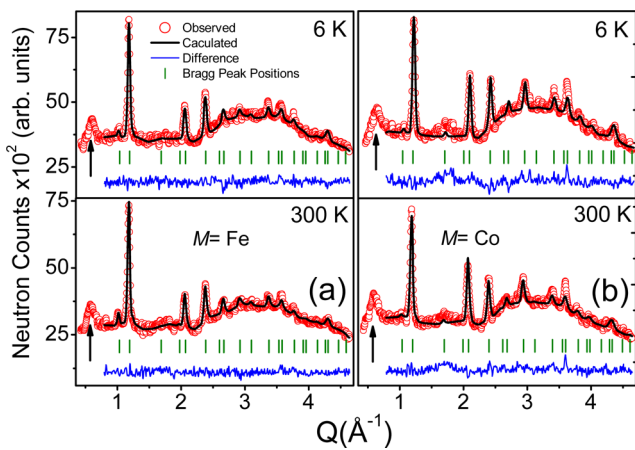


**Figure 9.** The Rietveld refined neutron diffraction patterns for both compounds  $\text{M}_{1.5}[\text{Cr}(\text{CN})_6]\cdot z\text{H}_2\text{O}$  ( $\text{M} = \text{Fe}$  and  $\text{Co}$ ) at 300 and 6 K. The open circles and solid lines indicate the observed and calculated patterns, respectively. The solid line at the bottom of each panel is the difference between observed and calculated patterns. The vertical lines at the bottom show the position of allowed nuclear Bragg peaks. The peak marked by an arrow in each panel indicates the forbidden Bragg peak (100) under  $Fm\bar{3}m$  space group.

the theoretically calculated spin only values for the  $\text{Fe}_{1.5}[\text{Cr}(\text{CN})_6]\cdot z\text{H}_2\text{O}$  and  $\text{Co}_{1.5}[\text{Cr}(\text{CN})_6]\cdot z\text{H}_2\text{O}$  compounds.

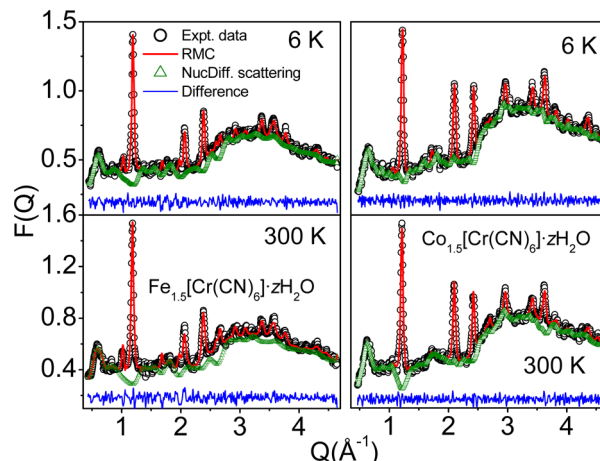


**Figure 10.** RMC calculated total scattering contribution of neutron diffraction patterns of  $\text{M}_{1.5}[\text{Cr}(\text{CN})_6]\cdot z\text{H}_2\text{O}$  ( $\text{M} = \text{Fe}$  and  $\text{Co}$ ) at 300 and 6 K. In each panel, the experimental neutron diffraction data, RMC calculated total scattering, and RMC calculated nuclear diffuse scattering are shown by the open circles, thick line, and open triangles, respectively. The solid line at the bottom of the curves shows the difference between the observed and the RMC calculated total intensities.

Figure 7 shows the magnetization as a function of the applied magnetic field at 1.6 K for  $\text{Fe}_{1.5}[\text{Cr}(\text{CN})_6]\cdot z\text{H}_2\text{O}$  and at 5 K for

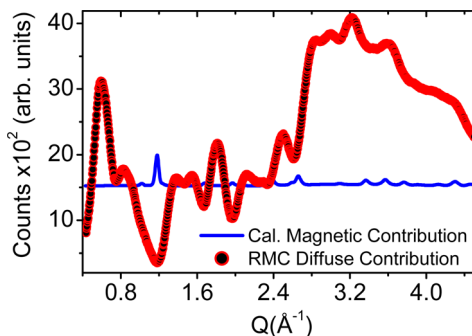


**Figure 11.** Comparison between the Rietveld method generated theoretical magnetic Bragg scattering contribution and RMC calculated total (nuclear + magnetic) diffuse scattering contribution for  $\text{Fe}_{1.5}[\text{Cr}(\text{CN})_6] \cdot z\text{H}_2\text{O}$  at 6 K.

$\text{Co}_{1.5}[\text{Cr}(\text{CN})_6] \cdot z\text{H}_2\text{O}$ . The hysteresis curves show the ferromagnetic nature of both compounds with a coercive field of 400 and 1200 Oe for  $\text{Fe}_{1.5}[\text{Cr}(\text{CN})_6] \cdot z\text{H}_2\text{O}$  and  $\text{Co}_{1.5}[\text{Cr}(\text{CN})_6] \cdot z\text{H}_2\text{O}$  compounds, respectively. The maximum magnetization is found to be 6.3 and 4.7  $\mu_{\text{B}}$ /f.u. for  $\text{Fe}_{1.5}[\text{Cr}(\text{CN})_6] \cdot z\text{H}_2\text{O}$  and  $\text{Co}_{1.5}[\text{Cr}(\text{CN})_6] \cdot z\text{H}_2\text{O}$  compounds, respectively. The theoretically expected (spin only) value of ordered magnetic moment  $\mu_s$  per formula unit is calculated by using the formula  $\mu_s = \sum(gnS)\mu_{\text{B}}$ , where  $g$  is the gyromagnetic ratio ( $\sim 2$ ),  $n$  is the number of magnetic ions with spin  $S$  in the formula unit, and the summation ( $\sum$ ) runs over all magnetic ions in the formula unit. For the  $\text{Fe}_{1.5}[\text{Cr}(\text{CN})_6] \cdot z\text{H}_2\text{O}$ , we have found from our Mössbauer study that 70.1% Fe ions are in high spin ( $t_{2g}^4 e_g^2, S = 2$ ) state, while 29.9% are in low spin ( $t_{2g}^6 e_g^0, S = 0$ ) state; the spin only ordered moment  $\mu_s$  should be  $\{2 \times 1.5 \times 2 \times 0.70 + 2 \times 1.5 \times 0 \times 0.30 + 2 \times 1 \times 3/2\} \mu_{\text{B}} = 7.2 \mu_{\text{B}}$  for ferromagnetic interaction between  $\text{Fe}^{\text{II}}$  and  $\text{Cr}^{\text{III}}$  ( $S = 3/2$ ) ions. Similarly, the spin only ordered moment  $\mu_s$  for the  $\text{Co}_{1.5}[\text{Cr}(\text{CN})_6] \cdot z\text{H}_2\text{O}$  compound should be  $7.5 \mu_{\text{B}}$ . The difference in the experimentally

observed and theoretically calculated ordered moment is due to the nonsaturation of the hysteresis curves up to 90 kOe for both compounds.

The microscopic nature of the magnetic ordering in such compounds can be understood from the superexchange interaction between transition metal ions (M) through the CN ligand. The superexchange interaction is ferromagnetic (FM) with ions of different orbital symmetries and otherwise antiferromagnetic (AFM). The possible exchange pathways between the orbital of  $\text{M}^{\text{II}}$  and  $\text{Cr}^{\text{III}}$  ions through the CN ligand are shown in Figure 8. Here, one can note that the electron transfer can only take place between the non-orthogonal orbitals. The  $e_g$  and  $t_{2g}$  orbitals of  $\text{M}^{\text{II}}$  ions are orthogonal to the  $2p_{\pi}$  and  $2p_{\sigma}$  orbitals of CN molecules, respectively. Therefore, the electron transfers from the  $\pi$  and  $\sigma$  orbitals of the CN molecule to the  $t_{2g}$  and  $e_g$  orbitals of  $\text{M}^{\text{II}}$  are only possible (shown by dotted lines in Figure 8). The remaining unpaired electrons in the  $e_g$  and  $t_{2g}$  orbitals of the  $\text{M}^{\text{II}}$  couple ferromagnetically or antiferromagnetically (depending upon their orbital symmetries) with the electrons in the  $t_{2g}$  orbital of  $\text{Cr}^{\text{III}}$  ions through the unpaired electrons in the  $\sigma$  or  $\pi$  orbitals of the CN molecule. Though both ferromagnetic (between  $e_g$  and  $t_{2g}$ ) as well as antiferromagnetic (between  $t_{2g}$  and  $t_{2g}$ ) interactions are possible between  $\text{Cr}^{\text{III}}$  ions ( $t_{2g}^3 e_g^0, S = 3/2$ ) and  $\text{M}^{\text{II}}$  ions [high spin  $\text{Fe}^{\text{II}}$  ions ( $t_{2g}^4 e_g^2, S = 2$ ) in  $\text{Fe}_{1.5}[\text{Cr}(\text{CN})_6] \cdot z\text{H}_2\text{O}$  (Figure 8a) and high spin  $\text{Co}^{\text{II}}$  ions ( $t_{2g}^5 e_g^2, S = 3/2$ ) in  $\text{Co}_{1.5}[\text{Cr}(\text{CN})_6] \cdot z\text{H}_2\text{O}$  (Figure 8b)], only the dominant one decides the magnetic structure and gets manifested in the experimental data. The ferromagnetic interaction between the  $e_g$  orbital of  $\text{Co}^{\text{II}}$  and the  $t_{2g}$  orbital of  $\text{Cr}^{\text{III}}$  ion is stronger than the antiferromagnetic interaction between the  $t_{2g}$  orbital of  $\text{Co}^{\text{II}}$  and the  $t_{2g}$  orbital of  $\text{Cr}^{\text{III}}$  (Figure 8b), confirming a ferromagnetic ordering in  $\text{Co}_{1.5}[\text{Cr}(\text{CN})_6] \cdot z\text{H}_2\text{O}$ .

**D. Neutron Diffraction Study: Reverse Monte Carlo Modeling.** To understand the microscopic nature of magnetic ordering in the two compounds, neutron powder diffraction

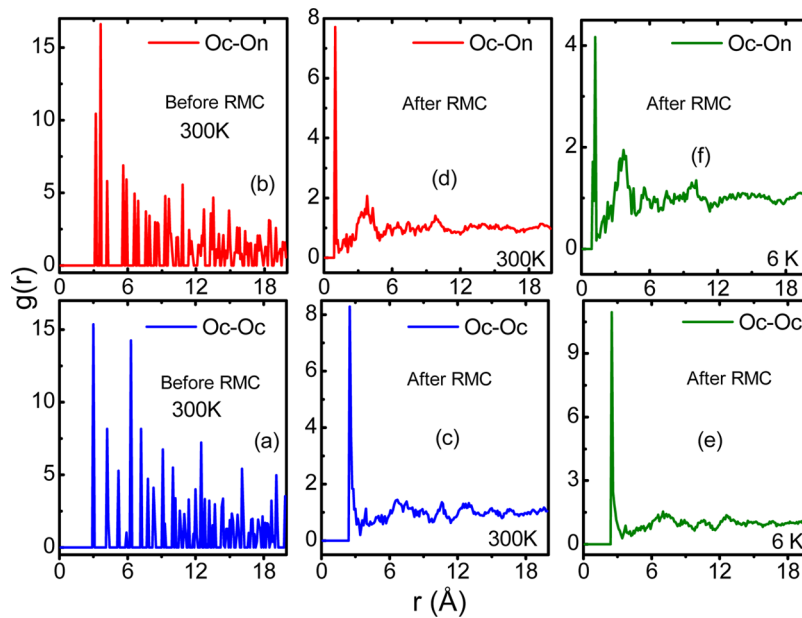


**Figure 12.** The partial pair correlation function  $g(r)$  with distance ( $r$ ) for for  $\text{Fe}_{1.5}[\text{Cr}(\text{CN})_6] \cdot z\text{H}_2\text{O}$  compound. Parts a and b show  $g(r)$  vs  $r$  at 300 K for the Oc—Oc (coordinated—coordinated) and Oc—On (coordinated—non-coordinated) oxygen atoms before RMC simulation. Parts c and d and e and f show  $g(r)$  vs  $r$  as obtained after RMC simulations at 300 and 6 K, respectively, for Oc—Oc and Oc—On oxygen atoms assuming the arrangement of these atoms as shown in Table 2.

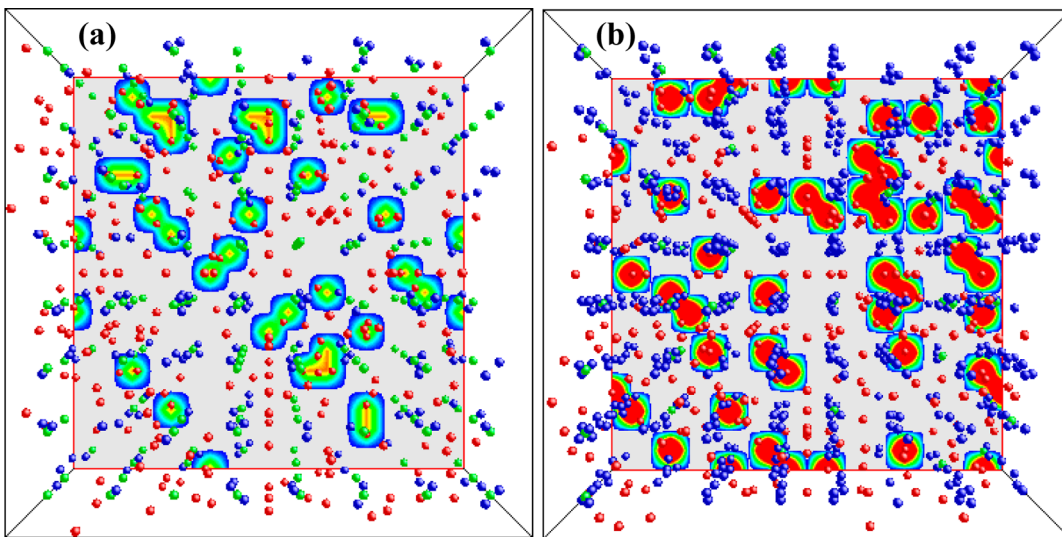


**Figure 13.** The distribution and arrangements of oxygen atoms before (a) and after (b) RMC simulation for the  $\text{Fe}_{1.5}[\text{Cr}(\text{CN})_6]\cdot z\text{H}_2\text{O}$  compound along the  $(x, 0, 0)$  direction. The 2D and contour plots are plotted together to visualize the oxygen clustering in a better way. The density of the oxygen atoms is maximum at the center, and it decreases toward the periphery.

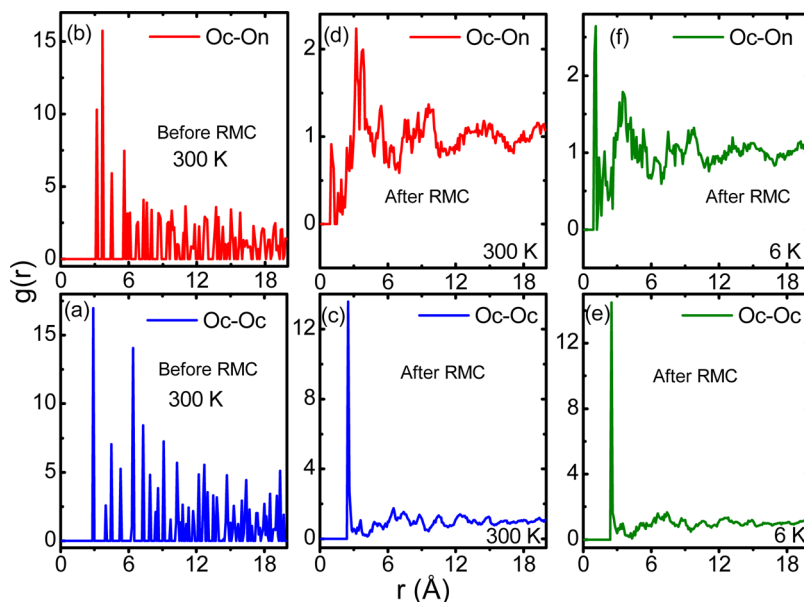


**Figure 14.** The partial pair correlation function  $g(r)$  with distance ( $r$ ) for  $\text{Co}_{1.5}[\text{Cr}(\text{CN})_6]\cdot z\text{H}_2\text{O}$  compound. The  $g(r)$  vs  $r$  at 300 K for the Oc—Oc (coordinated—coordinated) and Oc—On (coordinated—non-coordinated) oxygen atoms before RMC simulation are shown in parts a and b, whereas parts c and d and e and f show  $g(r)$  vs  $r$  as obtained after RMC simulations at 300 and 6 K, respectively, for Oc—Oc and Oc—On oxygen atoms.

patterns are recorded at room temperature and 6 K (which is well below the magnetic ordering temperature of both compounds). For structural analysis, the Fullprof program is employed which uses the Rietveld refinement method. The derived results are comparable with those obtained from the Rietveld refinement of X-ray diffraction patterns (Table 2). Figure 9 depicts the observed and Rietveld refined neutron diffraction patterns. It is interesting to note that the Bragg peak (100), marked by an arrow, is forbidden in the  $Fm\bar{3}m$  space group. Also, a large amount of diffuse scattering is present in the neutron diffraction patterns of both compounds, as can be seen by the modulations in the background. The presence of diffuse scattering and extra peak infers that there is an inherent structural disorder in the compounds. As mentioned in the Introduction, the standard methods of refining a diffraction pattern including the Rietveld

method do not provide information on the local structural correlations. Such information is contained in the diffuse scattering which is treated as a background by this method. Therefore, in order to extract useful information related to local structural correlations from the diffuse scattering, we have used the RMCPOW program<sup>44</sup> based on RMC simulations. This program has the ability to develop structural models of crystalline materials with local disorder, which are consistent with the experimental neutron diffraction data. The parameters obtained from the Rietveld analysis of neutron diffraction pattern have been used as an input in this program. Figure 10 shows the fitted RMCPOW patterns of neutron diffraction data for both compounds.  $F(Q)$ , the sum of the scattering amplitudes from all the atoms in the reciprocal space at a given  $Q$  value, is plotted. It is interesting to note that the forbidden Bragg peak (100) in

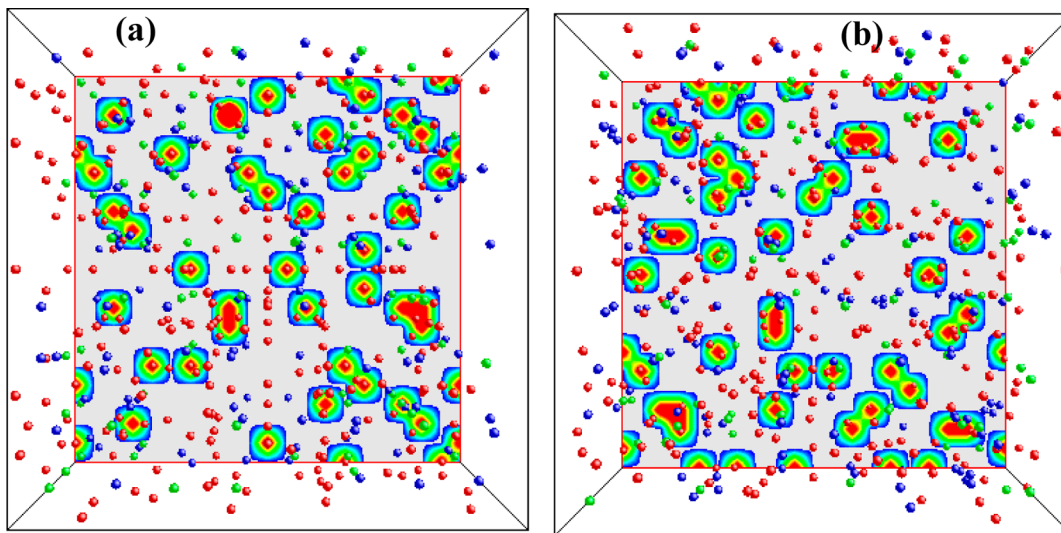


**Figure 15.** The distribution and arrangements of oxygen atoms before (a) and after (b) RMC simulation for the  $\text{Co}_{1.5}[\text{Cr}(\text{CN})_6] \cdot z\text{H}_2\text{O}$  compound along the  $(x, 0, 0)$  direction. The 2D and contour plots are plotted together to visualize the oxygen clustering in a better way. The density of the oxygen atoms is maximum at the center, and it decreases toward the periphery.

the neutron diffraction patterns has been fitted well by employing the RMC program for all patterns. This indicates that this peak is related to an inherent structural disorder in these compounds.

The neutron diffraction patterns recorded at 6 K (ferromagnetic phase for both compounds) do not show an enhancement in the intensity of fundamental (nuclear) Bragg peaks for both compounds. This is due to the reason that the magnetic contribution is orders of magnitude smaller than the nuclear diffuse scattering. In order to analyze the contribution from the diffuse scattering and the magnetic scattering qualitatively, we have plotted (in Figure 11) the total (nuclear + magnetic) diffuse scattering contribution obtained from the RMC analysis along with the Rietveld calculated magnetic Bragg intensity (assuming the theoretically expected ionic moments of  $4\mu_{\text{B}}$  and  $3\mu_{\text{B}}$  for  $\text{Fe}^{\text{II}}$  and  $\text{Cr}^{\text{III}}$ , respectively) for the  $\text{Fe}_{1.5}[\text{Cr}(\text{CN})_6] \cdot z\text{H}_2\text{O}$  compound. It is evident from the figure that the diffuse scattering contribution is substantially larger than the magnetic contribution, which makes the estimation of any magnetic Bragg intensity very difficult, even at a temperature much below the magnetic ordering temperatures. This is true for the  $\text{Co}_{1.5}[\text{Cr}(\text{CN})_6] \cdot z\text{H}_2\text{O}$  compound also.

The partial pair correlation function analysis provides information about the local crystal structure and is related to the probability of finding the center of an atom at a given distance from the center of another atom. Figure 12 shows the plots of partial pair correlation functions  $g(r)$  for the coordinated and non-coordinated oxygen atoms at 300 and 6 K for the  $\text{Fe}_{1.5}[\text{Cr}(\text{CN})_6] \cdot z\text{H}_2\text{O}$  compound. Figure 12a and b shows the  $g(r)$  before the RMC simulation (considering the periodic arrangement of O atoms, as obtained by Rietveld refinement) for coordinated-coordinated (Oc–Oc) and coordinated–non-coordinated (Oc–On) oxygen molecules for the  $\text{Fe}_{1.5}[\text{Cr}(\text{CN})_6] \cdot z\text{H}_2\text{O}$  compound at 300 K. It is seen that both coordinated (Oc) oxygen at the  $24e(x, 0, 0)$  site and non-coordinated (On) oxygen at the  $8c(1/4, 1/4, 1/4)$  and  $32f(x, x, x)$  sites are periodically arranged and lie over the range up to  $\sim 18\text{ \AA}$  in the configuration cell. However, the  $g(r)$  functions shown in Figure 12c and d for 300 K and 12e and f for 6 K, obtained after the RMC analysis, show confinement of oxygen atoms within the short distance. It is evident that the maximum number of Oc–Oc

pairs lies within a distance of  $\sim 4\text{ \AA}$  and the maximum number of Oc–On pairs lies within a distance of  $\sim 6\text{ \AA}$ , at both temperatures. The confinement of oxygen atoms within the short distance of  $\sim 4\text{ \AA}$  clearly suggests clustering of non-coordinated oxygen (On) around the coordinated oxygen (Oc) atoms. In order to visualize oxygen clustering, the distribution of atoms in the configuration cell has been depicted in Figure 13. It is seen that, before RMC simulation, the oxygen atoms are periodically distributed, shown by the yellow color intensity in the two-dimensional plot (Figure 13a). The oxygen clustering is clearly evident from the distribution of oxygen atoms in contour plots as well as from a two-dimensional plot, which shows the density of the oxygen atoms is maximum at the center (red color) and it decreases toward the periphery (cyan color) (Figure 13b).

Similarly, the plots of partial pair correlation functions  $g(r)$  for both oxygen atoms (Oc–Oc and Oc–On pairs) at 300 and 6 K for the  $\text{Co}_{1.5}[\text{Cr}(\text{CN})_6] \cdot z\text{H}_2\text{O}$  compound are shown in Figure 14. The  $g(r)$  functions (shown in Figure 14c and d for 300 K and 14e and f for 6 K) obtained after the RMC analysis show a clustering of oxygen atoms. At 300 K, the maximum number of Oc–Oc pair lies within a distance of  $\sim 3\text{--}4\text{ \AA}$  and the maximum number of Oc–On pairs lies within a distance of  $\sim 2\text{--}10\text{ \AA}$ . Similarly, the maximum number of Oc–Oc and Oc–On pairs for the compound at 6 K lies within a distance of  $\sim 3$  and  $\sim 2\text{--}10\text{ \AA}$ , respectively. The distribution of oxygen atoms in their two-dimensional plots has been shown in Figure 15. The oxygen clustering is evident, however not that prominent, to the  $\text{Fe}_{1.5}[\text{Cr}(\text{CN})_6] \cdot z\text{H}_2\text{O}$  compound, suggesting a lesser amount of local structural disorder in the  $\text{Co}_{1.5}[\text{Cr}(\text{CN})_6] \cdot z\text{H}_2\text{O}$  compound. Our IR study also supports the presence of less defects in the  $\text{Co}_{1.5}[\text{Cr}(\text{CN})_6] \cdot z\text{H}_2\text{O}$  compound compared to the  $\text{Fe}_{1.5}[\text{Cr}(\text{CN})_6] \cdot z\text{H}_2\text{O}$  compound. Thus, we have qualitatively and quantitatively investigated structural disorder in PBAs  $M_{1.5}[\text{Cr}(\text{CN})_6] \cdot z\text{H}_2\text{O}$  ( $M = \text{Fe}$  and  $\text{Co}$ ) using the RMC simulation on neutron diffraction data as well as correlated structural and magnetic properties. The observed correlation should be applicable and generic for the entire family of Prussian blue analogues of type  $A_q[\text{B}(\text{CN})_6]_r \cdot z\text{H}_2\text{O}$ .

## SUMMARY AND CONCLUSION

In summary, we have shown the advantage of RMC analysis in terms of the local atomic-scale structure and their correlations in  $M_{1.5}[\text{Cr}(\text{CN})_6] \cdot z\text{H}_2\text{O}$  ( $M = \text{Fe}$  and  $\text{Co}$ ) PBA compounds synthesized using the coprecipitation method. The XRD study shows that both compounds crystallize in the face-centered cubic crystal structure (space group  $Fm\bar{3}m$ ). The lattice parameters are found to be  $\sim 10.18(9)$  and  $10.38(3)$  Å for the  $\text{Fe}_{1.5}[\text{Cr}(\text{CN})_6] \cdot z\text{H}_2\text{O}$  and  $\text{Co}_{1.5}[\text{Cr}(\text{CN})_6] \cdot z\text{H}_2\text{O}$  compounds, respectively. The IR study confirms the formation of these PBAs, and Mössbauer study on  $\text{Fe}_{1.5}[\text{Cr}(\text{CN})_6] \cdot z\text{H}_2\text{O}$  confirms the presence of a high spin state ( $t_{2g}^4 e_g^2$ ,  $S = 2$ ) of  $\text{Fe}^{II}$  ions and flipping of  $\text{Cr}^{III}-\text{C}\equiv\text{N}-\text{Fe}^{II}$  to  $\text{Cr}^{III}-\text{N}\equiv\text{C}-\text{Fe}^{II}$ . The magnetization studies reveal a soft ferromagnetic nature of compounds with  $T_C$  values of  $\sim 17$  and  $\sim 22$  K for  $\text{Fe}_{1.5}[\text{Cr}(\text{CN})_6] \cdot z\text{H}_2\text{O}$  and  $\text{Co}_{1.5}[\text{Cr}(\text{CN})_6] \cdot z\text{H}_2\text{O}$ , respectively. The analysis of the RMC simulation study on  $M_{1.5}[\text{Cr}(\text{CN})_6] \cdot z\text{H}_2\text{O}$  compounds reveals that the occupation of the oxygen atoms at the empty  $\text{Cr}(\text{CN})_6$  sites is partially correlated which gives rise to the forbidden peak at the (100) Bragg position and the modulated background. In addition, the RMC analysis of the neutron diffraction data gives evidence of clustering of the non-coordinated oxygen atoms around the coordinated oxygen atoms in both compounds. The maximum number of coordinated-coordinated (Oc-Oc) and coordinated-non-coordinated (Oc-On) oxygen molecules lies within a distance of  $\sim 3-4$  and  $\sim 2-10$  Å for both compounds. We concluded that the water molecules and the  $[\text{Cr}(\text{CN})_6]$  vacancies are mainly responsible for the structural disorder present in these compounds.

## AUTHOR INFORMATION

### Corresponding Author

\*E-mail: prabhatt@barc.gov.in. Fax: +91 22 25505151.

### Present Address

<sup>†</sup>Department of Energy and Hydrocarbon Chemistry, Graduate School of Engineering, Kyoto University, Kyoto, Japan.

### Notes

The authors declare no competing financial interest.

## ACKNOWLEDGMENTS

The authors would like to thank Dr. A. Das and Ms. Neetika Sharma for their help in neutron diffraction measurements and Mr. P. Jha for IR measurement.

## REFERENCES

- (1) Popov, A. *Disordered Semiconductors: Physics and Applications*; Pan Stanford Publishing Pte. Ltd.: Singapore, 2011.
- (2) Xiao, G.; Cieplak, M. Z.; Gavrin, A.; Streitz, F. H.; Bakhshai, A.; Chien, C. L. *Phys. Rev. Lett.* **1988**, *60*, 1446–1449.
- (3) Sheng, Z. Z.; Hermann, A. M. *Nature* **1988**, *332*, 138–139.
- (4) Kudryavtsev, Y. V.; Oksenenko, V. A.; Lee, N. N.; Lee, Y. P.; Rhee, J. Y.; Dubowik, J. *J. Appl. Phys.* **2005**, *97*, 113903.
- (5) Lee, Y. P.; Kim, K. W.; Rhee, J. Y.; Kudryavtsev, Y. V. *Phys. Rev. B* **1999**, *59*, 546–553.
- (6) Singh, J. *Appl. Phys. Lett.* **1991**, *59*, 3142.
- (7) Schultz, A. J.; Wang, H. H.; Williams, J. M.; Filhol, A. *J. Am. Chem. Soc.* **1986**, *108*, 7853.
- (8) Petkov, V.; Billinge, S. J. L. Paper presented at the Conference: "From Semiconductors to Proteins: Beyond the Average Structure" held in Traverse City, Michigan, Aug 2001.
- (9) Petkov, V.; Jeong, I.-K.; Chung, J. S.; Thorpe, M. F.; Kycia, S.; Billinge, S. J. L. *Phys. Rev. Lett.* **1999**, *83*, 4089.
- (10) Jeong, I.-K.; Mohiuddin-Jacobs, F.; Petkov, V.; Billinge, S. J. L.; Kycia, S. *Phys. Rev. B* **2001**, *63*, 205202.
- (11) Petkov, V.; Billinge, S. J. L.; Larson, P.; Mahanti, S. D.; Vogt, T.; Rangan, K. K.; Kanatzidis, M. G. *Phys. Rev. B* **2002**, *65*, 092105.
- (12) Petkov, V.; Billinge, S. J. L.; Shastri, S. D.; Himmel, B. *Phys. Rev. Lett.* **2000**, *85*, 3436.
- (13) Seiler, P.; Dunitz, D. *Acta Crystallogr.* **1979**, *B35*, 1068.
- (14) Cao, D.; Bridges, F.; Anderson, M.; Ramirez, A. P.; Olapinski, M.; Subramanian, M. A.; Booth, C. H.; Kwei, G. H. *Phys. Rev. B* **2001**, *64*, 184409.
- (15) Mukadam, M. D.; Yusuf, S. M.; Sasikala, R.; Kulshreshtha, S. K. *J. Appl. Phys.* **2006**, *99*, 034310.
- (16) Mukadam, M. D.; Yusuf, S. M.; Sasikala, R. *J. Appl. Phys.* **2007**, *102*, 103902.
- (17) Dorset, D. L.; McCourt, M. P. *Acta Crystallogr.* **1994**, *A50*, 344.
- (18) Tokoroa, H.; Ohkoshi, S.-i. *Dalton Trans.* **2011**, *40*, 6825.
- (19) Ohkoshi, S. I.; Abe, Y.; Fujishima, A.; Hashimoto, K. *Phys. Rev. Lett.* **1999**, *82*, 1285.
- (20) Kumar, A.; Yusuf, S. M.; Keller, L.; Yakhmi, J. V. *Phys. Rev. Lett.* **2008**, *101*, 207206.
- (21) Sato, O.; Iyoda, T.; Fujishima, A.; Hashimoto, K. *Science* **1996**, *272*, 704.
- (22) Goodwin, A. L.; Chapman, K. W.; Kepert, C. J. *J. Am. Chem. Soc.* **2005**, *127*, 17980.
- (23) Ferlay, S.; Mallah, T.; Ouahes, R.; Veillet, P.; Verdaguer, M. *Nature* **1995**, *378*, 701.
- (24) Natesakhawat, S.; Culp, J. T.; Matranga, C.; Bockrath, B. *J. Phys. Chem. C* **2007**, *111*, 1055.
- (25) Reguera, L.; Balmaseda, J.; Castillo, L. F. d.; Reguera, E. *J. Phys. Chem. C* **2008**, *112*, 5589.
- (26) Thakur, N.; Yusuf, S. M.; Paulose, P. L.; Keller, L. *J. Appl. Phys.* **2012**, *111*, 063908.
- (27) Thakur, N.; Yusuf, S. M.; Yakhmi, J. V. *Phys. Chem. Chem. Phys.* **2010**, *12*, 12208.
- (28) Bleuzen, A.; Lomenech, C.; Escax, V.; Villain, F.; Varret, F.; Moulin, C. C. d.; Verdaguer, M. *J. Am. Chem. Soc.* **2000**, *122*, 6648.
- (29) Goujon, A.; Varret, F.; Escax, V.; Bleuzen, A.; Verdaguer, M. *Polyhedron* **2001**, *20*, 1339.
- (30) Tokoro, H.; Ohkoshi, S. *Progress in Nano-Electro-Optics VII Chemical, Biological, and Nanophotonic Technologies for Nano-Optical Devices and Systems*, 1st ed.; Springer: Berlin Heidelberg, 2010; Vol. 155.
- (31) Moritomo, Y.; Hanawa, M.; Ohishi, Y.; Kato, K.; Takata, M.; Kuriki, A.; Nishibori, E.; Sakata, M.; Ohkoshi, S.; Tokoro, H.; Hashimoto, K. *Phys. Rev. B* **2003**, *68*, 144106.
- (32) Ohkoshi, S.; Tokoro, H.; Hashimoto, K. *Coord. Chem. Rev.* **2005**, *249*, 1830.
- (33) Rietveld, H. M. *J. Appl. Crystallogr.* **1969**, *2*, 65.
- (34) Petkov, V.; Billinge, S. J. L.; Heising, J.; Kanatzidis, M. G. *J. Am. Chem. Soc.* **2000**, *122*, 11571.
- (35) Egami, T.; Billinge, S. J. L. *Underneath the Bragg peaks: structural analysis of complex materials*; Pergamon Press Elsevier: Oxford, England, 2003.
- (36) McGreevy, R. L.; Pusztai, L. *Mol. Simul.* **1988**, *1*, 359–367.
- (37) Rodriguez-Carvajal, J. *FULLPROF*, Nov 2007, website: <http://www ill.eu/sites/fullprof/>.
- (38) Keen, D. A.; Tucker, M. G.; Dove, M. T. *J. Phys.: Condens. Matter* **2005**, *17*, S15–S22.
- (39) Metropolis, N.; Rosenbluth, A. W.; Rosenbluth, M. N.; Teller, A. H.; Teller, E. *J. Phys. Chem.* **1953**, *21*, 1087.
- (40) McGreevy, R. L. *J. Phys.: Condens. Matter* **2001**, *13*, R877.
- (41) McGreevy, R. L.; Howe, M. A. *Annu. Rev. Mater. Sci.* **1992**, *22*, 217.
- (42) McGreevy, R. L.; Howe, M. A. *Annu. Rev. Mater. Sci.* **1992**, *22*, 217.
- (43) Mellergård, A.; McGreevy, R. L. *Acta Crystallogr., Sect. A* **1999**, *55*, 783.
- (44) Mellergård, A. *RMCPOW*, version 2.4; 2005-06-03; website: <http://www isis.rl.ac.uk/RMC/rmcpow.htm>.

- (45) Nakamoto, K. *Infrared and Raman Spectra of Inorganic and Coordination Compounds. Part B: Applications in Coordination, Organometallic and Bioinorganic Chemistry*, 5th ed.; Wiley-Interscience: New York, 1997.
- (46) Reguera, E.; Bertrán, J. F.; Nuñez, L. *Polyhedron* **1994**, *13*, 1619.
- (47) Kosaka, W.; Nomura, K.; Hashimoto, K.; Ohkoshi, S. *J. Am. Chem. Soc.* **2005**, *127*, 8590.
- (48) Arai, M.; Miyake, M.; Yamada, M. *J. Phys. Chem. C* **2008**, *112*, 1953.
- (49) Kumar, A.; Yusuf, S. M.; Keller, L.; Yakhmi, J. V.; Srivastava, J. K.; Paulose, P. L. *Phys. Rev. B* **2007**, *75*, 224419.
- (50) Brown, D. B.; Shriver, D. F.; Schwartz, L. H. *Inorg. Chem.* **1968**, *7*, 77.
- (51) Buschmann, W. E.; Ensling, J.; Gütlich, P.; Miller, J. S. *Chem.—Eur. J.* **1999**, *5*, 3019.
- (52) Shriver, D. F.; Shriver, S. A.; Anderson, S. E. *Inorg. Chem.* **1965**, *4*, 725.
- (53) Nuida, T.; Matsuda, T.; Tokoro, H.; Sakurai, S.; Hashimoto, K.; Ohkoshi, S.-i. *J. Am. Chem. Soc.* **2005**, *127*, 11604.
- (54) Coronado, E.; Giménez-López, M. C.; Korzeniak, T.; Levchenko, G.; Romero, F. M.; Segura, A.; García-Baonza, V. n.; Cezar, J. C.; Groot, F. M. F. d.; Milner, A.; Paz-Pasternak, M. *J. Am. Chem. Soc.* **2008**, *130*, 15519.
- (55) Ohkoshi, S.-i.; Hashimoto, K. *Chem. Phys. Lett.* **1999**, *314*, 210.
- (56) Greenwood, N. N.; Gibb, T. C. *Mössbauer Spectroscopy*; Chapman and Hall Ltd.: London, 1971.
- (57) Kumar, A.; Yusuf, S. M.; Keller, L. *Phys. Rev. B* **2005**, *71*, 054414.
- (58) Yusuf, S. M.; Rao, L. M. *J. Phys.: Condens. Matter* **1995**, *7* (29), 5891–5899.
- (59) Yusuf, S. M.; Sahni, V. C.; Rao, L. M. *J. Phys.: Condens. Matter* **1995**, *7*, 873.